Proceedings of the 21st ICSMGE, Vienna, Austria, 14 – 19 June 2026. Pistrol, Adam & Schweiger (eds.)
Published by: ÖGG, Austrian Society for Geomechanics, Salzburg, Austria, ISBN 978-3-9503898-4-5
https://doi.org/10.53243/ICSMGE2026-2387

Clarification of elastoplastic seabed behavior including liquefaction and subsequent solidification under continuous wave loading with its numerical reproduction

Takumi Iijima, Toshihiro Noda
Department of Civil and Environmental Engineering, Nagoya University, Japan, iijima.takumi.h3@s.mail.nagoya-u.ac.jp

ABSTRACT: The wave-induced elastoplastic seabed behavior from liquefaction to solidification (consolidation) observed in the experiments by Miyamoto et al. (2004) was reproduced using the soil-water coupled numerical analysis code ***GEOASIA***, which incorporates SYS Cam-clay model. Through the comparison between analytical results and the behavior observed in the experiments, we confirmed that the numerical analysis code can capture the following characteristics of the sequential wave-induced elastoplastic seabed behavior: quick and downward progress of liquefaction, gradual and upward progress of subsequent solidification, and large degree of compaction through solidification. Then, we clarified mechanisms of the seabed liquefaction and solidification by further looking at the analytical result as follows: Liquefaction occurred because plastic compression, which was induced quickly as if the sand bed were under undrained condition, reduced mean effective stress of the sand bed. The progress of liquefaction was faster in shallower regions, where the amount of plastic compression was larger. Conversely, the upward progress of solidification was explained by excess pore water pressure increasing linearly with depth, which caused the deepest elements adjacent to undrained bottom boundary to solidify first. Solidification propagated upward as excess pore water pressure dissipated from deeper regions, where the sand bed elements reached a heavily overconsolidated state. Because the continuous wave loading kept inducing plastic compression, solidification progressed slowly and the final total amount of compression became significantly large. Through this numerical study, it was found that the accumulation of plastic volume strain inside the normal yield surface, which is described by the subloading surface concept, is significant in terms of the numerical reproduction of the continuous elastoplastic seabed behavior due to waves.

KEYWORDS: Wave-induced seabed liquefaction, seabed consolidation, numerical analysis, elastoplasticity

1 INTRODUCTION

It has been observed in some experiments, e.g., Miyamoto et al. (2004), that under continuous ocean wave loading, seabed shows elastoplastic behavior including preceding liquefaction and subsequent solidification (consolidation). Understanding such sequential seabed behavior can be useful for estimating the physical condition of actual seabed, which in turn is helpful for design, construction, and assessment of offshore infrastructure based upon seabed foundations. To this end, numerical analysis methods have been utilized. However, in fact, validation of most of the previous numerical analysis methods was partial or inadequate as they focused only on seabed liquefaction (Ye et al. 2018) or employed inflexible constitutive relations between volumetric strain and the number of wave cycles, which cannot consider either various forms of wave loading or elastoplastic properties, e.g., density of soil (Miyamoto et al. 2004). Therefore, obtained insights from those numerical analysis methods may be limited.

The purpose of this research is to clarify mechanisms of the wave-induced elastoplastic seabed behavior including liquefaction and solidification using a validated numerical analysis method. For this purpose, we employed the ***u***-*p* formulation-based soil-water coupled finite deformation analysis code ***GEOASIA*** (Noda et al. 2008) incorporating SYS Cam-clay model (Asaoka et al. 2002). This constitutive model can reasonably consider elastoplastic properties of soil skeleton: overconsolidation, structure, and anisotropy, which are considered relevant to seabed behavior. In this paper, it will be shown that the numerical analysis code can express characteristics of the sequential wave-induced seabed behavior. Then, mechanisms of the wave-induced seabed liquefaction and solidification will be discovered by examining the numerical analysis results. Lastly, the important concept in the SYS Cam-clay model for reproducing the phenomena will be mentioned.

2 NUMERICAL REPRODUCTION OF THE WAVE-INDUCED ELASTOPLASTIC SEABED BEHAVIOR

Firstly in 2.1, characteristics of the sequential wave-induced seabed behavior including liquefaction and solidification observed in model experiments by Miyamoto et al. (2004) will be provided. Next in 2.2, details of the numerical analysis method and analysis conditions for numerical reproduction of the experimentally observed seabed behavior will be given. Comparison between the numerical and experimental results will be made in 2.3. Finally in 2.4, mechanisms of the wave-induced seabed liquefaction and solidification will be clarified by examining the numerical analysis result. The important concept in the elastoplastic constitutive model for describing the sequential wave-induced elastoplastic seabed behavior will be mentioned in 2.4.

2.1 *Sequential wave-induced elastoplastic seabed behavior observed in experiments by Miyamoto et al. (2004)*

Miyamoto et al. (2004) conducted 30g centrifugal model experiments, in which they applied cycles of progressive wave to a sand bed. Their apparatus is described in Figure 1. They measured water pressure at five vertical locations in the middle as depicted in Figure 1, one of which was set at the seabed surface to measure applied wave pressure and the other four labelled as A-D were placed inside the sand bed. For the experiment with application of 800 wave cycles, they determined time histories of excess pore water pressure u_e, which is defined as the gap between the measured pore water pressure and (constant) hydrostatic pressure, as shown in Figure 2. Additionally, they conducted upward seepage tests before and after the wave loading and obtained profiles of void ratio e shown in Figure 3. Notably, in these figures, time and length were multiplied by 30 following the similarity rule. By looking at these figures, they discovered the following characteristics of the wave-induced seabed behavior:

- Quick and downward progress of liquefaction

Figure 2 shows that excess pore water pressure u_e at the four locations A-D increased quickly after the application of wave loading and liquefaction, which was considered to have occurred when u_e reached initial vertical effective stress σ'_{v0}, took place faster at the shallower location, i.e., downward progress of liquefaction.

- Gradual and upward progress of solidification

Figure 2 also shows that u_e gradually decreased after liquefaction while wave loading continued. This decrease in u_e was considered to have been accompanied by consolidation (called "solidification" in their study). Furthermore, it can be seen that the decrease in u_e started faster at deeper locations, suggesting that solidification proceeded upwards.

- Large degree of compaction during solidification

Figure 3 shows reduction in void ratio e at the four locations through the experiment with 800 wave loading cycles. This means that the sand bed compressed (solidified) all over the depth. In fact, this amount of compression was much larger than the one after consolidation under a calm water level, which was realized in another experiment by halting wave loading when the upper half was considered to have not solidified yet and letting u_e dissipate under a calm water level. Therefore, it was concluded that solidification, i.e., consolidation under continuous wave loading, was accompanied by a larger degree of compaction than the consolidation without wave loading.

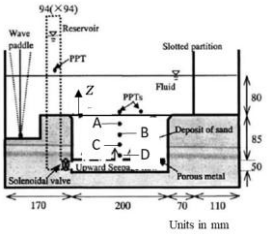

Figure 1. Experimental apparatus of Miyamoto et al. (2004) with the four locations labeled as A-D. *1

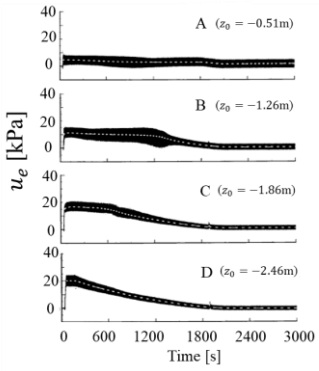

Figure 2. Time histories of excess pore water pressure in the experiment by Miyamoto et al. (2004). *1*2

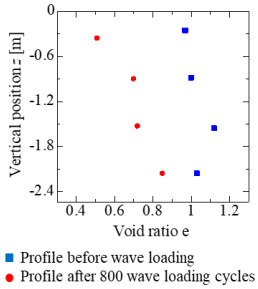

Figure 3. Void ratio profiles before and after the experiment with 800 wave loading cycles by Miyamoto et al. (2004). *1*2

*1 The original figures from Miyamoto (2003) are modified.

*2 Time and length are multiplied by 30 from the experimental values.

2.2 *Numerical analysis method and analysis condition*

We employed the soil-water coupled numerical analysis code ***GEOASIA*** (Noda et al. 2008), which incorporates the elastoplastic constitutive model, the SYS Cam-clay model (Asaoka et al. 2002), to reproduce the sequential elastoplastic seabed behavior including liquefaction and subsequent solidification observed in the experiments by Miyamoto et al. Key features of the numerical analysis method are summarized as follows:

- $\boldsymbol{u}$-p formulation with a rate-type equation of motion were adopted.
- Soil displacements $\boldsymbol{u}$ were nodally discretized with FEM and pore water pressures p were elementally discretized with FVM.
- Implicit time discretization scheme based on Wilson's θ method was adopted.
- Finite deformation was considered.
- Permeability coefficient k_s was dependent on void ratio e according to the Taylor (1948)'s equation, i.e., $k_s = C_f \mathrm{e}^3/(1+\mathrm{e})$, where C_f was a constant.
- Compressibility of pore fluid due to existence of pore air was considered with bulk modulus of pore fluid K_f.
- Variable soil states of overconsolidation, structure, and anisotropy were considered with the SYS Cam-clay model.

The numerical model is described in Figure 4. The model was 30 times larger than the sand bed of the experiments following the similarity rule. In Figure 4, horizontal and vertical coordinates, x and z, and the four locations, where excess pore water pressure will be focused, were defined in alignment with the experiments. As for the boundary conditions, they were also aligned with the experiments as side and bottom boundaries were undrained and displacements normally to the boundaries were prohibited while parallel displacements were unrestrained. Normally to the sand bed surface, progressive wave loading (both water pressure and normal total stress) p_s were applied as $p_s = p_o \sin(kx - \omega t) + \gamma_w(H_w - z_b)$, where p_o, k, and ω are wave pressure amplitude, wave number ($k = 2\pi/L$; L is wavelength), and angular frequency ($\omega = 2\pi/T$; T is wave period), respectively; γ_w (=9.81 kPa) is the unit weight of water; H_w (=2.4 m) is water depth in a calm state; z_b is a vertical position of the seabed surface. Since this numerical analysis code considers finite deformation, the boundary wave pressure could vary according to deformation of the sand bed surface. All analytical conditions including wave properties, soil properties, elastoplastic parameters, evolution parameters, and initial condition variables are listed in Table 1. The wave characteristics were obtained from the analysis of Miyamoto et al., while the wavelength L was estimated from the dispersion relation of the linear wave theory, $L = \mathrm{g}T^2/2\pi \tanh(2\pi H_w/L)$, where g (=9.81 m/s^2) is the gravitation acceleration. Among the soil properties, (initial) permeability coefficient k_s, the coefficient for the Taylor's equation, and soil particale density ρ_s were obtained from the analysis of Miyamoto et al. Poisson's ratio ν, elastoplastic parameters and evolution parameters were conformed to the ones of Tani et al. (2015) as their analyses utilized fitted parameters of Silica sand No.7, which was also used in the experiments by Miyamoto et al. The only exception was degradation index of overconsolidation m, which was smaller than that of Tani et al. to consider a significant amount of plastic compression. The bulk modulus of pore fluid K_f was obtained from a model analysis condition introduced by Japan Society of Civil Engineers (1994). Note that corresponding degree of saturation S_r was 99.8%. As for the initial values of state variables, specific volume v_0 corresponding to the relative

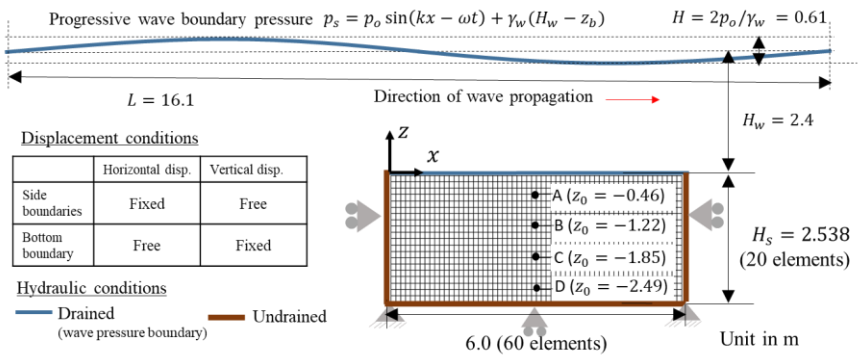

Figure 4. Numerical model and boundary conditions

Density D_r=30% was consistent for all the soil elements to be aligned with the experiments. We considered that degree of structure $1/R_0^*$, degree of anisotropy ζ_0, and stress ratio η_0 were also consistent in the sand bed, therefore overconsolidation ratio $1/R_0$ (OCR) was distributed vertically.

Table 1. Parameters for numerical analysis.

Wave properties	
Wave pressure amplitude p_o [kPa]	3.0
Wave period T [s]	3.75
Wavelength L [m] *1	16.1
Soil properties	
(Initial) permeability coefficient k_s [m/s]	1.9×10^{-4}
Coefficient of Taylor's equation C_f [m/s]	3.5×10^{-4}
Soil particle density ρ_s [kg/m^3]	2.69×10^{3}
Poisson's ratio ν	0.15
Bulk modulus of pore fluid K_f [kPa] *2	4.24×10^{4}
Elastoplastic parameters	
NCL intercept N	1.980
Critical state index M	1.200
Compression index $\tilde{\lambda}$	0.045
Swelling index $\tilde{\kappa}$	0.002
Evolution parameters	
Degradation index of overconsolidation m *3	0.02
Degradation index of structure a (b=c=1.0)	2.2
Degradation index of structure c_s	1.0
Rotational hardening index b_r	3.5
Limitation of rotational hardening m_b	0.9
Initial conditions	
Specific volume v_0	2.033
Degree of structure $1/R_0^*$	2.0
Overconsolidation ratio (OCR) $1/R_0$ *4	-
Degree of anisotropy ζ_0	0.545
Stress ratio η_0	0.545

*1 Estimated from the linear wave theory.
*2 Corresponding to degree of saturation S_r to be 99.8%.
*3 Reduced from the value of Tani et al. (2015).
*4 Calculated from other parameters.

2.3 *Results of numerical analysis*

In Figure 5, time histories of excess pore water pressure u_e at the four locations in the experiment and this numerical analysis are compared. Figure 5 shows that the numerical method could reproduce the sequential elastoplastic seabed behavior observed in the experiment as both quick build-up of u_e (liquefaction) and gradual reduction in u_e (solidification) throughout the depth are observed. Figure 6 compares vertical profiles of void ratio e before and after wave loading in the experiment and the numerical analysis. Focusing on the profiles after the wave loading, the numerical method could reproduce the significant

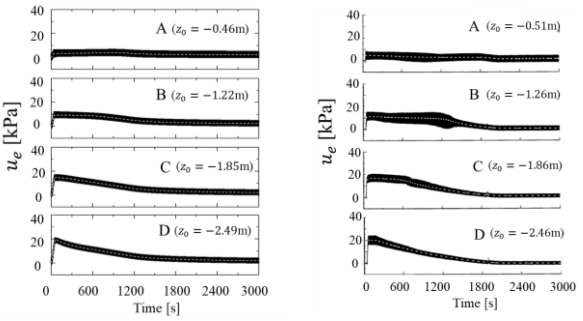

a) Numerical result of this study b) Experimental result by Miyamoto et al. (2004)

Figure 5. Time histories of excess pore water pressure at the four vertical locations.

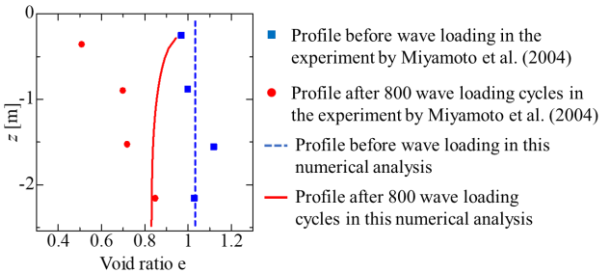

Figure 6. Void ratio profiles before and after wave loading.

reduction in e, i.e., compaction, especially near the sand bed bottom as observed in the experiment.

To identify the progression direction of liquefaction and solidification in the numerical analysis, Figure 7 showing the time histories of two liquefaction indices at the four locations is examined. The two indices are excess pore water pressure ratio u_e/σ'_{v0} (σ'_{v0}: initial vertical effective stress), and mean effective stress ratio p'/p'_0 (p': mean effective stress and p'_0: its initial value). In this study, we consider that liquefaction occurred when $u_e/\sigma'_{v0} > 0.9$ or $p'/p'_0 < 0.1$. Looking at the initial changes of the two indices described in Figure 7a) and 7b), liquefaction occurred from the shallower location A and it expanded to the deeper locations B, C, D in this order. Therefore, the downward progress of liquefaction could be reproduced. Notably, this is due to a relatively large amount of plastic compression induced in the shallower region because the plastic compression triggered liquefaction as explained in 2.4.

Focusing on the latter phase of solidification, in which u_e/σ'_{v0} decreased and p'/p'_0 increased, Figure 7c) shows that after liquefaction, u_e/σ'_{v0} decreased and deviated downward from the 90% line from the deepest location D and this was followed by the shallower locations B, C, A in this order.

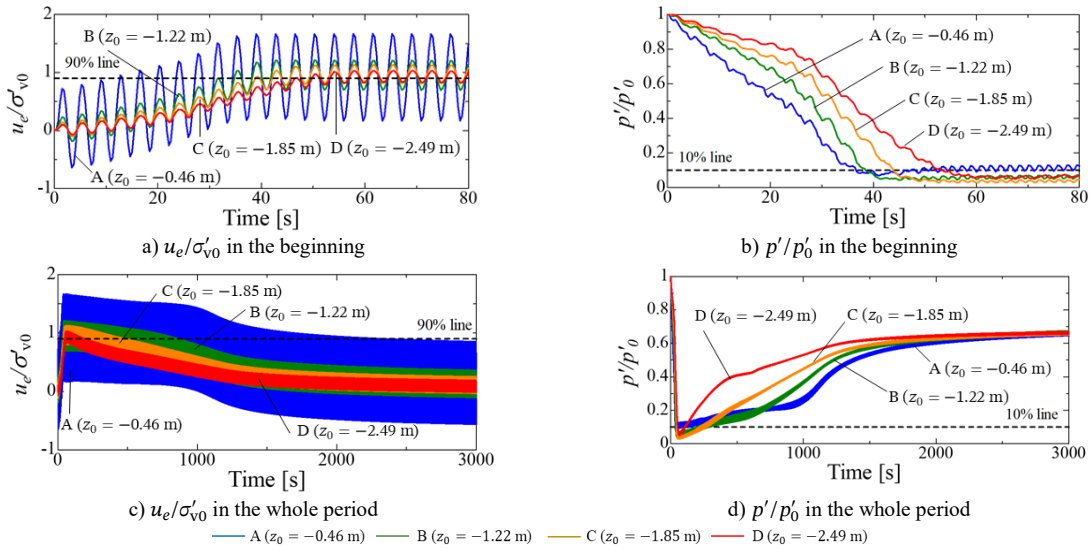

Figure 7. Time histories of excess pore water ratio u_e/σ'_{v0} and mean effective stress ratio p'/p'_0 in the beginning and the whole period.

However, Figure 7d) shows that p'/p'_0 first increased at the shallowest location A deviating upward from the 10% line, then increased at the deepest location D, C, B in this order. This means that withdrawal from liquefaction was fastest at the shallowest location A, although p' recovered slowly at A. Considering these results, we concluded that completion of solidification progressed upward, although the shallowest part could withdraw from liquefaction faster than the deeper parts.

2.4 *Mechanisms of liquefaction and solidification*

The mechanisms of wave-induced seabed liquefaction and solidification observed in the experiments by Miyamoto et al. (2004) are clarified by investigating the results of the numerical analysis validated in the previous section.

Firstly, we looked at typical behavior of the sand bed element at the location B ($z_0 = -1.22$ m) subjected to the 800 wave loading cycles as depicted in Figure 8, where the relation between mean effective stress ratio p'/p'_0 and deviator stress ratio q/p'_0 (q is deviator stress) and the relation between p'/p'_0 and specific volume v are shown. Focusing on the initial phase of wave loading, both p'/p'_0 and q/p'_0 decreased as a trend and eventually the element underwent liquefaction as p'/p'_0 became smaller than 10%. During this “liquefaction” phase, specific volume v did not change as if the element were in undrained condition. This absence of volume change can be attributed to the short period of time for pore water to flow and excess pore water pressure to dissipate. After a while, the element experienced solidification as both p'/p'_0 and q/p'_0 increased. During this “solidification” phase, specific volume decreased significantly, which means that the elements underwent significant plastic compression.

Next, we further examined the elemental behavior, which was typical in each phase. As shown in Figure 9a) and 9b), the time histories of boundary wave pressure p_b, q/p'_0, plastic volume strain ε_v^p (compression: positive), p'/p'_0, and excess pore water pressure ratio u_e/p'_0 are described for the same sand bed element at location B when the number of wave cycles was 0-2 for the liquefaction phase and 300-302 for the solidification phase, respectively. Looking at Figure 9a), we aimed to explain the mechanism of the seabed liquefaction specifically focusing on its quickness and downward progress as follows: As wave loading acted on the sand bed, positive plastic volume strain ε_v^p was generated through loading inside the normal yield surface and under the Critical State Line by the role of subloading surface (Hashiguchi, 1978; 1989). And particularly in the beginning when the soil elements were still loose, a large amount of positive ε_v^p was generated. During this "liquefaction" phase, the time was so short that the pore water could not flow yet, i.e., under nearly undrained condition, and thus the total volumetric strain ε_v remained zero. According to the additive decomposition of volumetric strain, $\varepsilon_v = \varepsilon_v^p + \varepsilon_v^e$ (ε_v^e: elastic volume strain), negative elastic volume strain ε_v^e, which causes elastic expansion, had to emerge. Then, according to the elastic constitutive equation, $\Delta p' = K\Delta\varepsilon_v^e$ (K is bulk modulus of soil skeleton expressed as $= \mathrm{v}p'/\tilde{\kappa}$; Δ denotes an incremental amount), mean effective stress p' had to decrease. This was accompanied by build-up of excess pore water pressure u_e following the principle of effective stress, $\Delta p = \Delta p' + u_e$ (p: mean total stress). Specifically, because the external force, i.e., wave load on the seabed surface, was a periodic load with a steady amplitude, Δp was approximately zero and $\Delta p'$ was negative. As for the mechanism of downward progress of liquefaction, it can be explained as follows. Figure 10 illustrates isochrones of vertical distribution of initial mean effective stress p'_0 and plastic volume strain ε_v^p in the liquefaction phase at $t = 30$ s (t is the elapsed time) when around 8 wave cycles were applied. It was found that the element at the shallower location A recorded the largest ε_v^p in the liquefaction phase, which was followed by the deeper elements at B, C, D in this order. Liquefaction began at the shallower location A and propagated towards the deeper elements B, C, and D due to the small initial mean effective stress p'_0 in the shallower region.

Looking at the sand bed behavior during the solidification phase shown in Figure 9b), the mechanism is revealed focusing particularly on its slowness, upward progression, and large degree of compaction. Firstly, the reason why the solidification occurred is explained. Figure 11 shows the isochrones of the vertical distribution of the total head h (the sum of the vertical position z and the pore water pressure divided by the unit weight of pore water u_w/γ_w), the overconsolidation ratio OCR, and the void ratio e at different times during the liquefaction phase and the solidification phase. Looking at Figure 11a), the total head kept increasing during the liquefaction phase due to the accumulated excess pore water pressure u_e. The total head recorded its maximum value in most regions when liquefaction completed at around $t = 57$s denoted by the green line. At this time, the total head distribution showed almost linear increase

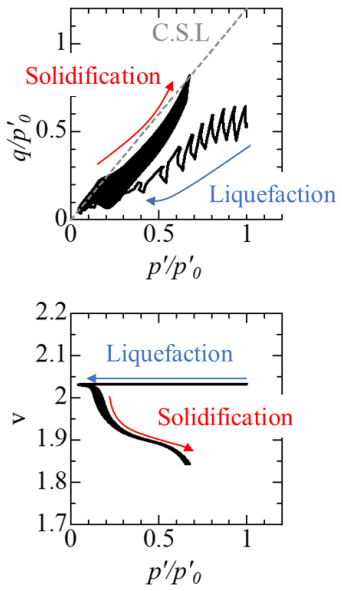

Figure 8. Elemental behavior at location B

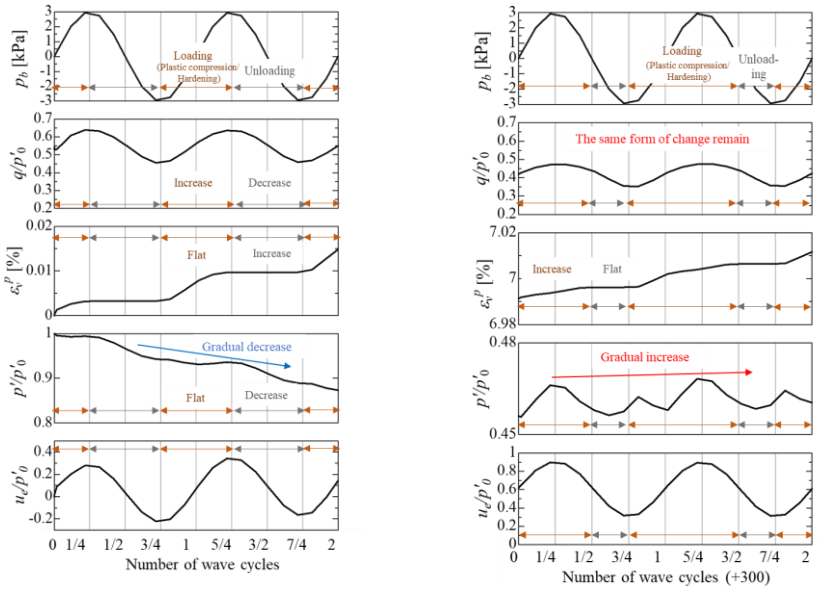

a) in the liquefaction phase b) in the solidification phase

Figure 9. Time histories of variables in the two phases at location B.

in h with depth because u_e compensated the complete loss of initial mean effective stress. Therefore, pore water had to flow upward uniformly, namely most of the soil elements did not need to consolidate (solidify) by reducing inner pore water since the net amounts of vertical pore water discharge were zero. However, the exception was the element adjacent to the undrained bottom boundary because it had to consolidate by providing pore water upward as there was no pore water flow from underneath. This is how the solidification started from the deepest element. After u_e dissipated in the deepest element and reached a largely overconsolidated state, at which the upward provision of pore water declined because of the smaller ε_v^p generated, the second deepest element also solidified to sustain the upward pore water flow. This timing can be seen in the isochrones at $t = 180$ s shown as the light green line in Figure 11b). Similarly, the other shallower elements also experienced solidification after the end of solidification in deeper elements as an example represented by the orange line at $t = 799$ s. This is how solidification progressed upward. Eventually, solidification completed in all the elements with the gradient of total head throughout the depth becoming insignificant and ceased upward pore water flow as depicted by the red lines at $t = 3000$ s. Secondly, the reason why the solidification occurred slowly and accompanied the large degree of compaction is explained. Looking at Figure 9b), plastic volume strain ε_v^p kept increasing because of the continuous wave loading causing constant fluctuation of effective stress q/p'_0. This constant accumulation of ε_v^p prevented recovery of p' and dissipation of u_e for the same mechanism of liquefaction explained above. Therefore, solidification had to progress slowly and resulted in the large degree of compaction due to the large amount of ε_v^p.

Note that the accumulation of ε_v^p turned out to play a crucial role in reproducing both liquefaction and solidification. This is realized by the subloading surface model as mentioned above.

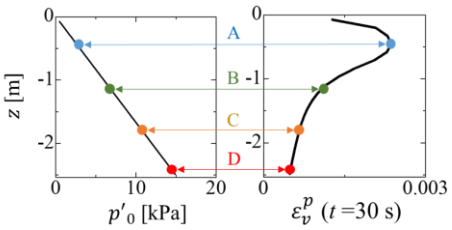

Figure 10. Isochrones of initial mean effective stress p'_0 and plastic volume strain ε_v^p at $t = 30$ s.

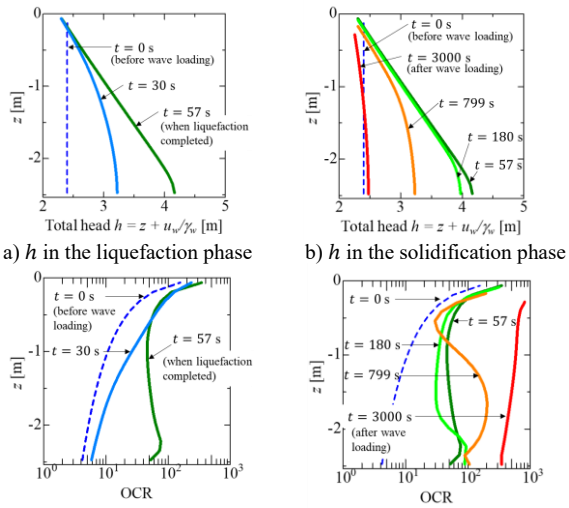

a) h in the liquefaction phase b) h in the solidification phase

c) OCR in the liquefaction phase d) OCR in the solidification phase

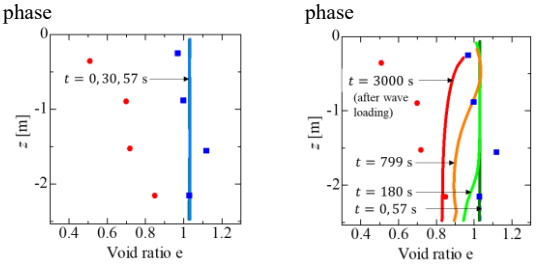

e) e in the liquefaction phase f) e in the solidification phase

Figure 11. Isochrones of vertical distributions of variables

3 CONCLUSION

The sequential wave-induced elastoplastic seabed behavior including liquefaction and subsequent solidification observed in the experiments by Miyamoto et al. (2004) was numerically reproduced with the soil-water coupled analysis code ***GEOASIA*** incorporating the SYS Cam-clay model. It was confirmed that the following three characteristic behaviors could be reproduced in the numerical analysis: quick and downward progress of liquefaction, gradual and upward progress of solidification, and large degree of compaction through solidification. In addition, mechanisms of the wave-induced liquefaction and solidification were clarified by looking closely at the numerical analysis result as follows:

- Liquefaction occurred due to plastic compression caused by wave loading in a substantially undrained condition. The liquefaction progressed downward because plastic volume strain ε_v^p was larger at shallower locations where initial mean effective stress p_0' was smaller.
- When liquefaction took place throughout the entire depth, p_0' was replaced by excess pore water pressure u_e and uniform upward pore water flow occurred according to the almost uniform total head distribution. Solidification started from the deepest elements because they were adjacent to the undrained bottom boundary and needed to solidify by supplying inner pore water upward. After u_e dissipated in the deepest elements and they solidified into a heavily overconsolidated state with the amount of generated ε_v^p becoming insignificant, the second deepest elements had to solidify to sustain the upward pore water flow. Similarly, solidification occurred in the shallower elements as well and ended when all the elements solidified with ceased upward pore water flow.
- Throughout the solidification process, accumulation of ε_v^p continued due to the continuous wave loading, which prevented the recovery of the mean effective stress. Therefore, solidification progressed slowly and accompanied significant compaction.

Note that the accumulation of ε_v^p inside the normal yield surface is ascribed to the role of the subloading surface, and therefore, this model turned out to be vital in numerical reproduction of the sequential wave-induced elastoplastic seabed behavior.

4 ACKNOWLEDGEMENTS

This study was supported by JSPS KAKENHI (grant number: 22K14324) and involved extensive discussions with Dr. Tomohiro Toyoda.

5 REFERENCES

Asaoka, A., Noda, T., Yamada, E., Kaneda, K., and Nakano, M. 2002. An elasto-plastic description of two distinct volume change mechanisms of soils. *Soils and Foundations* 42(5), 47-57.

Hashiguchi, K. 1978. Plastic constitutive equations of granular materials. In *Proc. US-Japan Seminar on Contimuum Mech. Stast. Appr. Mech. Granular Materials,* Sendai*,* 321-329.

Hashiguchi, K. 1989. Subloading surface model in unconventional plasticity. *International journal of solids and structures*, 25(8) 917-945.

Japan Society of Civil Engineers 1994. Coastal wave. 432-510 (in Japanese).

Miyamoto, J. 2003. The dynamics of liquefied sand under wave loading with applications to nearshore engineering. [Doctoral thesis, Kyoto University]. *Kyoto University.*

Miyamoto, J., Sassa, S., and Sekiguchi, H. 2004. Progressive solidification of a liquefied sand layer during continued wave loading. *Geotechnique* 54(10), 617-629.

Noda, T., Asaoka, A., and Nakano, M. 2008. Soil-water coupled finite deformation analysis based on a rate-type equation of motion incorporating the SYS Cam-clay model. *Soils and Foundations* 48(6), 771-790.

Tani, K., Kiyota, T., Matsushita, K., Hashimoto, T., Yamamoto, A., Takeuchi, H., Noda, T., Kiku, H., and Obayashi, J. 2015. Liquefaction countermeasures by shallow ground improvement for houses and their cost analysis. *Soil Dynamics and Earthquake Engineering* 79, 401-414.

Taylor, D. W. 1948. Fundamentals of soil mechanics. Wiley, New York.

Ye, G. L., Leng, J., and Jeng, D. S. 2018. Numerical testing on wave-induced seabed liquefaction with a poro-elastoplastic model. *Soil Dynamics and Earthquake Engineering* 105, 150-159.